

Multi-level, Forming Free, Bulk Switching Trilayer RRAM for Neuromorphic Computing at the Edge

Jaeseoung Park¹, Ashwani Kumar¹, Yucheng Zhou¹, Sangheon Oh¹, Jeong-Hoon Kim¹, Yuhan Shi¹, Soumil Jain², Gopabandhu Hota¹, Amelie L. Nagle³, Catherine D. Schuman⁴, Gert Cauwenberghs² and Duygu Kuzum^{1*}

¹Department of Electrical and Computer Engineering, ²Department of Bioengineering, University of California, San Diego, CA, USA. ³Department of Computer Science, Massachusetts Institute of Technology, MA, USA. ⁴Department of Electrical Engineering and Computer Science, University of Tennessee, TN, USA.

The authors contributed equally: Jaeseoung Park, Ashwani Kumar.

* Corresponding Author: Duygu Kuzum, email: dkuzum@ucsd.edu

Abstract—Resistive memory-based reconfigurable systems constructed by CMOS-RRAM integration hold great promise for low energy and high throughput neuromorphic computing. However, most RRAM technologies relying on filamentary switching suffer from variations and noise leading to computational accuracy loss, increased energy consumption, and overhead by expensive program and verify schemes. Low ON-state resistance of filamentary RRAM devices further increases the energy consumption due to high-current read and write operations, and limits the array size and parallel multiply & accumulate operations. High-forming voltages needed for filamentary RRAM are not compatible with advanced CMOS technology nodes. To address all these challenges, we developed a forming-free and bulk switching RRAM technology based on a trilayer metal-oxide stack. We systematically engineered a trilayer metal-oxide RRAM stack and investigated the switching characteristics of RRAM devices with varying thicknesses and oxygen vacancy distributions across the trilayer to achieve reliable bulk switching without any filament formation. We demonstrated bulk switching operation at megaohm ($M\Omega$) regime with high current nonlinearity and programmed up to 100 levels without compliance current. We developed a neuromorphic compute-in-memory platform based on trilayer bulk RRAM crossbars by combining energy-efficient switched-capacitor voltage sensing circuits with differential encoding of weights to experimentally demonstrate high-accuracy matrix-vector multiplication. We showcased the computational capability of bulk RRAM crossbars by implementing a spiking neural network model for an autonomous navigation/racing task. Our work addresses challenges posed by existing RRAM technologies and paves the way for neuromorphic computing at the edge under strict size, weight, and power constraints.

Introduction

As the Moore's law is coming to an end due to the limitations of physical scaling of CMOS technology, neuromorphic compute-in-memory (CIM) approaches have attracted huge attention to keep improving computing performance¹. The CIM has the potential to alleviate the von Neumann bottleneck, a limitation in computing performance resulting from significant energy loss and time delays during data transfer between processors and memory units in classical computing systems. While GPUs and tensor processing units excel in parallel computing compared to CPUs, they are still reliant on static random access memory, which demands substantial physical space^{2,3}. Emerging non-volatile memory (eNVM) devices including phase change memory (PCM)⁴, magnetic random access memory (MRAM)⁵, conductive bridge random access memory (CBRAM)^{6,7}, ferroelectric field effect transistor (FeFET)⁸, resistive random access memory (RRAM)^{9,10}, and memristive synapses based on 2D materials¹¹⁻¹³ have been extensively studied for physical implementations of neuromorphic CIM platforms. RRAM devices are gaining attention due to their exceptional density, lower fabrication cost, and back-end-of-line (BEOL) compatibility with CMOS technology^{9,14}.

RRAM-based reconfigurable systems hold great promise for low energy and high throughput neuromorphic computing. Neurosynaptic cores constructed by CMOS-RRAM integration have shown dynamically high-performance reconfigurable dataflow and energy efficiency of 74 TMACS/W^{15,16}. However, three major challenges are yet to be addressed to scale CMOS-RRAM based accelerators and achieve energy-efficient dynamic on-chip learning with RRAM crossbar arrays: (i) Most of the RRAM devices rely on filamentary switching, which suffers from extensive variations and noise leading to computational accuracy loss and increased energy consumption¹⁷. Programming RRAM into multi-level resistance states requires expensive read and verify programming schemes, unsuitable for on-chip training^{18,19}. (ii) Low ON-state resistance of filamentary RRAM increases the power consumption due to high current read and write operations. As the resistance approaches the interconnect resistance²⁰, it constrains the array size and parallel multiply & accumulate (MAC) operations. (iii) Filamentary RRAM

requires high forming voltages to generate a conductive filament, that is not compatible with advanced CMOS technology nodes. To address all these challenges, here, we demonstrate systematic engineering of a trilayer metal-oxide bulk RRAM stack and investigate the switching characteristics of RRAM devices with varying thicknesses and V_O distributions across the trilayer. Sputtered porous TiO_x layer facilitates modulation of V_O distribution in the switching layer without forming V_O filaments (Fig. 1a), enabling bulk switching operations in the megaohm ($M\Omega$) range, achieving high current nonlinearity, and programming up to 100 levels without the need for compliance current. Highly linear MVMs are achieved by using the row-differential scheme instead of non-differential scheme in fabricated bulk RRAM crossbars²¹. We employ the fabricated RRAM crossbars to perform control for an autonomous navigation/racing task using a spiking neural network (SNN) model, demonstrating compatibility for neuromorphic computing at the edge applications. Our work tackles the challenges presented by current filamentary RRAM technologies, clearing a path for neuromorphic computing at the edge while adhering to stringent size, weight, and power constraints.

Results

Optimization of trilayer bulk RRAM stack

To systematically investigate switching characteristics of RRAM devices based on multi-layer stacks, we fabricated RRAM devices in four different switching layers ($Al_2O_3/TiO_2/TiO_x$) configurations (**Table 1**). Our detailed fabrication process is explained in the methods. All samples include 3nm Al_2O_3 as a high bandgap tunnel barrier ($E_g \sim 9.0eV$) layer to limit the current and provide I-V nonlinearity through tunneling. For S1 and S2, ALD TiO_2 layers (S1 = 20nm, S2 = 40nm) were deposited without breaking the vacuum. S3 and S4 have 3nm ALD TiO_2 and sputtered TiO_x layers (S3 = 6.5nm, S4 = 40nm) with varying oxygen stoichiometry (**Fig. 1a**). As shown in the plane-view and cross-sectional SEM images, 16×16 crossbar arrays were fabricated using a via-hole structure design (**Fig. 1b, c, d**). The via-hole structure was chosen to achieve uniform and reliable device switching instead of simple crossbar structure. The via-hole

design with 150nm thick plasma-enhanced chemical vapor deposition (PECVD) SiO₂ insulator eliminates the edge effects due to high-field corners or sidewalls²². In addition, all steps of the fabrication process have low thermal budget ($T < 300^{\circ}\text{C}$) which is perfectly compatible with CMOS BEOL integration process.

We first tested DC switching characteristics for all samples. Both S1 (**Fig. 1e**, $R_{\text{on}} = 150\Omega$, $R_{\text{off}} = 400\text{k}\Omega$) and S2 (**Fig. 1f**, $R_{\text{on}} = 3\text{k}\Omega$, $R_{\text{off}} = 2\text{G}\Omega$) exhibit only filamentary switching with significant variations in set/reset voltages in consistent with the previous research on the filamentary RRAM using Al₂O₃/TiO_{2-x} stacks⁹. The high OFF-state resistance of S2 is due to thicker TiO₂ layer. A 200 μA compliance current is necessary to prevent permanent breakdown during DC set process for both devices. Although the filamentary RRAM shows resistance switching behavior, these devices suffer from highly non-uniform switching characteristics due to the stochastic nature of filament formation and rupture¹⁷. The low ON-state resistance of the filamentary RRAM also increases the power consumption due to high energy read and write operations. In addition, the abrupt resistance jumps during the set and reset processes are not suitable for continuous synaptic weight updates during online learning where the multi-level conductance update is needed. RRAM devices including sputtered TiO₂ (S3) or TiO_x (S4) layer exhibit bulk switching characteristics (**Fig. 1g, h**). Surprisingly, S3 shows both filamentary and bulk switching with a transition from filamentary switching to bulk switching as DC sweep range is decreased from 1.5 V to 1 V. In high voltage DC sweep range ($|V| < 1.5\text{ V}$) where filamentary switching is observed, it follows the same switching polarity (a positive set and negative reset voltage) as S1 and S2 filamentary RRAM devices ($R_{\text{on}} = 200\Omega$, $R_{\text{off}} = 145\text{k}\Omega$). In low voltage DC sweep range ($|V| < 1\text{V}$) where bulk switching dominates, it demonstrates gradual resistance change during DC sweep without any sudden resistance jumps that are observed in filamentary switching ($R_{\text{on}} = 76\text{k}\Omega$, $R_{\text{off}} = 180\text{k}\Omega$). Switching direction for bulk switching (a negative voltage set and a positive voltage reset) show opposite polarity to filamentary switching. Although both filamentary and bulk switching are observed in different voltage regimes and the opposite polarity, coexistence of both mechanisms is not desirable for reliable synaptic weight updates²³. For the RRAM devices with a thicker and V_O-rich sputtered TiO_x layer (S4), only bulk switching behavior is observed without any filament

formation. S4 exhibits, highly reliable bulk switching behavior with excellent uniformity over 50 DC cycles (**Fig. 1h**, $R_{on} = 410k\Omega$, $R_{off} = 1M\Omega$). Furthermore, the bulk switching for S4 exists in the $M\Omega$ resistance range in contrast to bulk switching occurring $\sim 100k\Omega$ for S3. Therefore, we decided to further investigate switching characteristics and multi-level resistance states for the trilayer bulk RRAM (S4) and chose it for neuromorphic computing with the crossbar array demonstrations.

To analyze trilayer structure of the bulk switching RRAM, the transmission electron microscopy (TEM) and scanning transmission electron microscopy - electron energy loss spectroscopy (STEM-EELS) analyses were performed (**Fig. 2**). The ALD TiO_2 layer has darker contrast in bright field-TEM image, confirming higher atomic density than the TiO_x layer (**Fig. 2a**). STEM-EELS line-scan profile shows lower oxygen concentration in TiO_x layer than ALD TiO_2 layer (**Fig. 2b**). Furthermore, STEM-EELS composition map (**Fig. 2c**) shows nm-scale dark areas only in the sputtered TiO_x layer pointing to a porous structure. To further analyze the crystal structure and film density, grazing incidence X-ray diffraction (GIXRD) and X-ray reflection (XRR) measurements were conducted (**Fig. S1**). 30nm ALD TiO_2 layer shows crystalline anatase phase while sputtered TiO_x films show an amorphous phase. The grain boundaries are well known to be the high diffusivity paths of small ions such as oxygens or hydrogens^{24,25}. Especially in polycrystalline filament RRAM devices, the grain boundaries acts an important role in charge transport and V_O accumulation and diffusion²⁶. Due to these diffusivity paths, filament formation and rupture easily occur in the filamentary RRAM devices (S1 and S2). In the amorphous phase, however, there are no high diffusivity paths for V_O , so the filament formation can be successfully suppressed. XRR measurements show that the critical angle of sputtered TiO_x layer (0.52°) is smaller than ALD TiO_2 layer (0.55°), suggesting that the film mass density is smaller for the sputtered TiO_x layer. The distribution of V_O defects is modulated by the external electric field in a whole switching layer rather than forming a locally accumulated V_O filaments, so that we can achieve bulk switching behavior.

Characterization of bulk RRAM switching behavior

Observing uniform and forming free bulk switching in the trilayer RRAM with oxygen deficient TiO_x layer, we investigated the area scaling of the device resistance to confirm bulk switching (**Fig. 3a-d**, Diameter: $3\mu\text{m} - 10\mu\text{m}$). For the trilayer RRAM (S4), Resistance linearly scales with the area for both high resistance (HRS) and low resistance states (LRS) (**Fig. 3b**), suggesting bulk switching^{23,27}. In the filamentary RRAM, both HRS and LRS resistances are independent on the device area because the resistance depends on the width and conductivity of the filament that can only be modulated by the compliance current during the SET process²⁸. The device-to-device (D2D) variations of pristine, HRS, and LRS states show tight distributions in $\text{M}\Omega$ regime (**Fig. 3c, d**), addressing the high variability issue of filamentary RRAM devices. Perfectly overlapping DC sweeps over 50 cycles (Fig. 1 h) suggest that the trilayer bulk RRAM exhibits minimal cycle-to-cycle variation.

We systematically studied the conduction mechanism of trilayer bulk RRAM by fitting DC I-V characteristics with direct tunneling, Fowler-Nordheim (FN) tunneling and space-charge-limited conduction (SCLC) models in both HRS and LRS (**Fig. 3e-h**). To investigate the conduction mechanism in the bulk RRAM devices, the I-V characteristics are plotted in a $\log(I/V^2)$ vs. $1/V$ form (**Fig. 3f**). In this plot, there are two different voltage regime where the direct tunneling and Fowler-Nordheim (FN) tunneling dominate by the following equations, where g is the tunneling gap, m^* is the effective mass, ϕ is the barrier height, \hbar is Planck' constant, and q is the elementary charge²⁹.

$$\text{Direct tunneling, } I \propto V \cdot \exp\left(\frac{-2g\sqrt{2m^*\phi}}{\hbar}\right)$$

$$\text{FN tunneling, } I \propto V^2 \cdot \exp\left(\frac{-4g\sqrt{2m^*\phi^3}}{3\hbar qV}\right)$$

In a low voltage regime ($V < 0.06\text{V}$), the current of both HRS and LRS states are linear to the voltage, meaning that the direct tunneling is the dominant conduction mechanism. In a high voltage regime ($V > 0.5\text{V}$), however, the $\log(I/V^2)$ is linear to the $1/V$, where the FN tunneling becomes dominant. These

tunneling conduction occurs through the high band gap Al_2O_3 layer which provides the $\text{M}\Omega$ -level resistance switching and high nonlinearity ($I_V / I_{0.5V} = 15$ ($V = 1.5\text{V}$)) of I-V curves³⁰. Both HRS and LRS states of bulk RRAM devices follow the same conduction mechanism, whereas the filamentary RRAM or CBRAM would show ohmic conduction in LRS states because current conduction occurs through the V_O or metal cation filaments^{29,31}. To study the switching mechanism, the double-log plot of I-V curves were fitted with the SCLC theory³² (**Fig. 3g**). In the low voltage regime, the double-log I-V curves follow a linear relationship due to the dominance of the direct tunneling ($I \propto V$). In the mid voltage regime, they follow a quadratic relation due to the trap-limited conduction through the V_O deep defects in the sputtered TiO_x layer ($I \propto V^2$). In the high voltage regime, $\log I - \log V$ dependence suggests the trap-filling modulated conduction ($I \propto V^\alpha$, $\alpha > 2$). The trap-filled limit voltage (V_{TFL}), the voltage where the trap filling starts, can be extracted from the SCLC fitting results (**Fig. 3h**). The trap density (N_t) can be calculated using the following equation, where N_t is the trap density, L is the thickness, and ϵ is the dielectric constant³².

$$V_{\text{TFL}} = qN_tL^2/2\epsilon$$

Trap-filled limit voltage (V_{TFL}) of different resistance states calculated from the SCLC fitting shows that the trap density (N_t) is decreased as the device resistance is increased (**Fig. 3h**). The proposed mechanism for bulk switching is explained as follows (**Fig. 1a**): resistance is changed through modulation of the V_O distribution in the porous TiO_x rather than the formation of V_O filaments that would connect the top electrode to the bottom electrode through the switching layer. A positive voltage applied to the top electrode pushes positively charged V_O away from TiO_x layer, reducing V_O concentration and the electric field across Al_2O_3 tunnel barrier. This results in the reduction of tunneling current and the resistance increase of bulk RRAM. The bulk switching shows the opposite polarity to the filamentary switching consistent with other previous reports^{23,33}.

The ability to perform analog weight updates is a crucial feature in synaptic devices for efficient implementation of learning and inference in neuromorphic computing applications. Analog weight update is

the most important property in synaptic devices to achieve successful neuromorphic computing applications. The filamentary RRAM shows abrupt resistance change so that they have been mainly employed for binary or low-precision implementation of neural network weights. Programming filamentary RRAM devices into discrete conductance states require extensive number of program and verify operations, not suitable for online learning applications²⁷. In contrast, for the bulk RRAM devices, it is easier to achieve gradual weight updates. We first investigated gradual weight updates using identical pulses in two different conductance regimes; $\sim 0.8 \mu\text{S}$ and $\sim 0.12 \mu\text{S}$. 32-states are achieved by applying of identical set and reset pulses for both conductance regimes (**Fig. 4a, b**). The long-term potentiation (LTP) and the long-term depression (LTD) curves show gradual conductance change ($V_{\text{read}} = 0.1\text{V}$). We also implemented an incremental pulse scheme. We optimized the incremental pulse scheme to have linear LTP and LTD curves with a higher dynamic range and larger number of states (**Fig. 4c**). **Fig. 4d and 4e** show the gradual current increase/decrease during the transient set (-2.0V)/reset ($+1.5\text{V}$) pulses. Based on all the pulse measurement results, the trilayer RRAM devices show gradual conductance switching in $\text{M}\Omega$ regime that can overcome the drawbacks of filamentary RRAM devices which show binary resistance states in $\text{k}\Omega$ regime. Endurance and read disturbance are tested up to 200k cycles and they show no degradation in device characteristics due to uniform and stable bulk RRAM switching (**Fig. S2**).

Hardware SNN implementation with RRAM crossbars

For the hardware implementation of neural networks, we first investigated the effect of ON and OFF state resistances (R_{ON} and R_{OFF}) on the read and write operations across crossbar arrays using circuit simulations (HSPICE). **Fig. S3a** shows that for $R_{\text{OFF}} < \sim 10 \text{M}\Omega$, the read margin significantly degrades as the array size increases. For the write operation, the voltage across individual RRAM cells decreases with R_{ON} (**Fig. S3b**). These results indicate the importance of $\text{M}\Omega$ range resistance to maintain read and write accuracy for selector-less crossbars. Although $\text{M}\Omega$ resistance and nonlinearity of trilayer RRAM are great for reliable crossbar operation, a small dynamic range ($R_{\text{ON}}/R_{\text{OFF}} \sim 2.5$) is a limiting factor. To address that,

we employed a row-differential encoding scheme (**Fig. 5a**), where two RRAMs represent positive and negative weights by utilizing opposite voltage polarity, i.e., $V_{WL+} = V_{ref} + V_{READ}$, $V_{WL-} = V_{ref} - V_{READ}$. The differential conductance ‘Diff_G’ given by $G^+ - G^-$, represents both positive and negative weights. For the differential read of multi-level RRAM, the effective dynamic range depends on the minimum achievable conductance difference ($Diff_G_{min}$) as in equation ‘ $2(G_{max} - G_{min}) / Diff_G_{min}$ ’ (**Fig. 5a**). It results in a significantly higher dynamic range (~ 170) compared to the non-differential single RRAM scheme (**Fig. 5b**) due to the small ‘ $Diff_G_{min}$ ’, helping with mapping a wider range of real-valued weights. For hardware implementation with RRAM crossbar arrays, we developed a neuromorphic compute-in-memory platform (**Fig. 5d**). It utilizes a switched capacitor voltage-sensing circuit to avoid the need for current-sensing schemes relying on high-power large-area transimpedance amplifiers (**Fig. 5e, f**)³⁴. We performed read (**Fig. 5g**) and MVM computations on the trilayer RRAM crossbar and demonstrated the differential scheme can achieve highly linear MVM computation.

For neuromorphic computing at the edge with trilayer bulk RRAM crossbars, we implemented an SNN trained using Evolutionary Optimization for Neuromorphic Systems (EONS) algorithm³⁵. In EONS algorithm, randomly generated populations are used as initial seeds for neural network optimizations. The fitness score, a criterion to measure how accurate the neural network is, is assessed in each neural network during the evaluation step. Then, the selected networks through the tournament methods are used to perform reproduction steps where various operators occur (e.g., duplication, crossover, and mutation). In this research, the SNN was specifically trained for a small-scale autonomous racing task³⁶ using LIDAR sensor data as the input and producing speed and steering angle as the outputs. For the evolutionary training, the fitness function was defined to evaluate the spiking neural network and to encourage behaviors for completing the task without colliding with a wall³⁶. The SNN was trained on 5 Formula-1 tracks and tested on an additional 15 tracks (representative tracks are shown in **Fig. 6a**)³⁷, performing pruning after the training. The pruned SNN consists of 14 input neurons and 30 output neurons including recurrent connectivity across and within the layers (**Fig. 6b**). For the hardware demo, SNN weights were quantized

into 4-bit precision and mapped onto RRAM arrays according to the row-differential scheme. Experimentally mapped weights onto the crossbar show high consistency with the ideal (target) weight map (**Fig. 6c**). **Fig. 6e** and **6f** show steering angle and speed calculated based on experimental RRAM weights in comparison to software simulation during autonomous navigation testing of the Catalunya map. Quantitative comparison of speed and steering angle computations during navigation through all 15 racetracks show great agreement with the ideal software simulation of the SNN (**Fig. 6d**).

Discussion

In this work, we successfully demonstrated a forming-free and bulk switching RRAM technology by engineering a trilayer metal-oxide stack. We systematically optimized the trilayer oxide stacks which consist of high bandgap tunneling barrier (Al_2O_3) and different stoichiometric TiO_2 and TiO_x layers. Due to the highly porous and amorphous TiO_x layer, V_O filament formation was effectively suppressed, whereas the crystalline TiO_2 layer showed filamentary switching characteristics. We achieved multi-level, uniform bulk switching in $\text{M}\Omega$ regime without a compliance current. This bulk RRAM technology can address the limitations of filamentary RRAM technologies such as high device variability, low ON-state resistance, and need for high forming voltage.

In addition, we developed a neuromorphic CIM platform using bulk RRAM crossbars by combining energy-efficient switched-capacitor voltage sensing circuits with differential encoding of weights. The row-differential weight encoding enabled to increase dynamic range of bulk RRAM devices as well as to give high-accuracy MVM operations. We successfully mapped weights of SNN network for autonomous navigation/racing tasks on Formula-1 racetracks onto bulk RRAM crossbars using the row-differential weight encoding scheme. The fitness score of weight maps on crossbars hardware showed good agreement with ideal software simulation results, suggesting a computational capability of bulk RRAM crossbars. Our work addresses the problems of the filamentary RRAMs and offers a promising pathway towards energy-efficient dynamic on-chip learning with RRAM crossbars.

Methods

Bulk RRAM fabrication and packaging crossbars.

Ti (12nm) / Au (100nm) bottom electrode was deposited by the sputtering on a 4-inch SiO₂ (300nm) / Si wafer with bilayer lift-off process (LOR5B and AZ1512). Plasma-enhanced chemical vapor deposition (PECVD) SiO₂ (150nm) layer was deposited as an insulating interlayer dielectric layer. Various via-hole sizes (Diameter: 3μm to 10μm) were patterned with maskless photolithography and inductively coupled plasma etching process with CF₄ atmosphere. The Al₂O₃ / TiO₂ (3nm / 3nm) atomic layer deposition (ALD) layer was deposited with trimethyl aluminum (TMA) and titanium chloride (TiCl₄) precursor and water oxidant without breaking vacuum. The sputtered TiO_x layer was deposited with sputtering under the different oxygen partial pressures to induce the V_O into the film (S3: 100W, O₂/(O₂+Ar) = 10% / S4: 200W, O₂/(O₂+Ar) = 5%). Ti (12nm) / TiN (22nm) / Ti (12nm) / Au (200nm) top electrode was deposited and patterned analogous to the bottom electrode lift-off process. The switching layer was etched away by plasma etching processed with O₂ / CF₄ / Ar / BCl₃ gas chemistry. The Au wire bonding was done using manual west bond ball bonder equipment.

Materials characterization

For structural characterization, high-resolution X-ray scattering measurements (Grazing Incidence X-ray diffraction and X-ray reflection) were conducted using in-house X-ray diffraction (Smartlab XRD, Rigaku). Transmission electron microscopy (TEM)-ready samples were prepared using the in-situ FIB lift-out technique on an FEI Dual Beam FIB/SEM. The samples were capped with sputtered Ir and e-Pt/I-Pt prior to milling. The TEM lamella thickness was ~100nm. The samples were imaged with a FEI Tecnai TF-20 FEG/TEM operated at 200kV in bright-field (BF) TEM mode, high-resolution (HR) TEM mode, and high-angle annular dark-field (HAADF) STEM mode. The STEM probe size was 1-2nm nominal diameter.

Electrical characterization and weight mapping on crossbars.

The electrical I-V characteristics of the RRAM devices were measured using a semiconductor analyzer (4155C, Agilent) and switching matrix (E5250A, Keysight). A pulse generator unit (81110A, Agilent) and pulse measurement units with remote amplifiers (4200-SCS with 4225-PMU and 4225-RPM, Keithley) were used for the pulse generation and measurements.

The bulk RRAM crossbar arrays were wire-bonded on pin grid arrays and mounted on custom designed printed circuit board (PCB) to map the weights on the arrays. Weight mapping process on the arrays was conducted using connected switching matrix, semiconductor analyzer, and a pulse generator unit. We implemented an Opal Kelly FPGA Board to demonstrate the voltage sensing scheme³⁴. The conductance was calculated by driving WLs to V_{pulse} and measuring the time constant of BL charging. Then the absolute conductance was calculated by the following expression.

$$V_{BL} \approx V_{ref} + \frac{g_i}{\sum_{k=1}^N g_k} V_{pulse}, \text{ for } t \gg \frac{C}{\sum_{k=1}^N g_k}$$

Formula-1 track simulation.

We leveraged the TENNLab Neuromorphic Framework software framework³⁸, along with Evolutionary Optimization for Neuromorphic Systems (EONS)³⁵ to design a spiking neural network for evaluation in our hardware. The task that we optimized the neural network for was autonomous control of a small-scale autonomous race car. We leveraged the F1Tenth³⁹ simulation environment for training. In this environment, the observations provided to the neural network as input are LIDAR observations from the car, and the actions that can be applied (that are produced as output by the network) are steering angle and speed.

We defined discrete values that the network can choose for steering angles ([0,-0.01,0.01,-0.03,0.03,-0.05,0.05,-0.07,0.07, -0.1, 0.1, -0.13, 0.13, -0.15, 0.15, -0.17, 0.17, -0.2, 0.2, -0.23,0.23, -0.25, 0.25, -0.27, 0.27, -0.3, 0.3, -0.34, 0.34]) and speed ([1, 1.1, 1.2, 1.3, 1.4, 1.5, 1.6, 1.7, 1.8, 1.9, 2]). Two sets of output neurons are created, one for steering angle and one for speed, and within those sets, one for each legal value. At each step of the simulated environment, the car receives as input 10 LIDAR beams, down-selected from the full 960 LIDAR beams by selecting the maximum beam distance in each of ten equal-sized regions of the 960 beams. Then, the network simulates for 50 time steps, and the output neuron that fires most for

steering angle corresponds to the selected steering angle value (and similarly for speed). Observations are taken and actions are applied of 2 milliseconds in the simulation. Thus, the network makes decision about steering angle and speed every 2 milliseconds.

Following methods similar to those in³⁶, we used EONS to optimize the parameters (synaptic weights and neuron thresholds) and structure (number of hidden neurons and connectivity between neurons) of a single spiking neural network. EONS is an evolutionary algorithm-based approach that begins with an initial population of randomly initialized networks. Then, each network is evaluated to determine a training score. These scores are used with tournament selection to preferentially select better-performing networks to serve as parents. Then, new networks are created from those parents through recombination/crossover and random mutations. The new population is then evaluated, and this process is repeated for a fixed number of generations. In this case, we optimized a single network for 200 generations. The training performance of the network that is used to drive the optimization is the average score across five real-world Formula 1 tracks, where the score for each track is the percentage of two laps completed without crashing. The testing score of the network is the average score across fifteen other Formula 1 tracks (i.e., tracks not used during training). In this previous work, we have seen that the networks trained in simulation are frequently able to translate to successfully operate a small-scale physical autonomous car.

Acknowledgements

This work was supported by the Office of Naval Research (N000142012405) and the Quantum Materials for Energy Efficient Neuromorphic Computing (Q-MEEN-C), an Energy Frontier Research Center (EFRC), funded by the US Department of Energy, Office of Science, Basic Energy Sciences under award #DE-SC0019273.

Sample	Oxide Stack	Dominating Switching
S1	ALD Al ₂ O ₃ / TiO ₂ (3nm / 20nm)	Filamentary
S2	ALD Al ₂ O ₃ / TiO ₂ (3nm / 40nm)	Filamentary
S3	ALD Al ₂ O ₃ / TiO ₂ (3nm / 3nm) / Sputter TiO ₂ (6.5nm)	Filamentary / Bulk
S4	ALD Al ₂ O ₃ / TiO ₂ (3nm / 3nm) / Sputter TiO _x (40nm)	Bulk

Table 1. Four different multilayer stacks are fabricated (S1-S4). Only the trilayer with a sputtered TiO_x layer (S4) shows bulk switching characteristics.

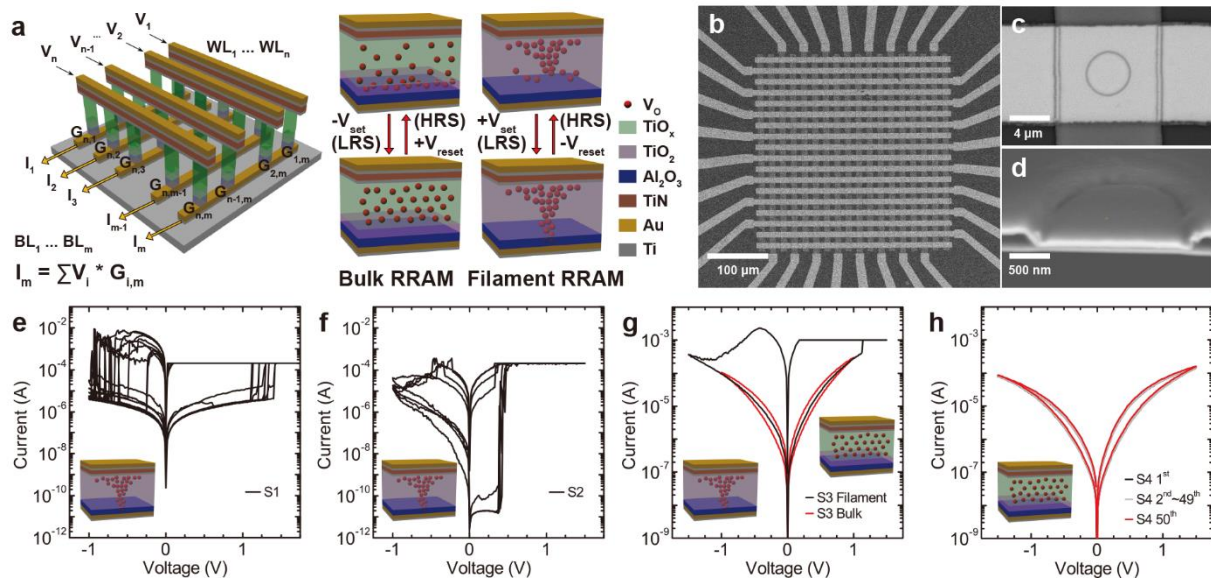


Figure 1. RRAM device stack and DC I-V switching characterization. **a.** Illustration of fabricated RRAM device stack and crossbar arrays. Bulk and filamentary RRAM switching mechanisms are compared. For bulk switching, the distribution of oxygen vacancies (V_O) is modulated between TiO_x and TiO_2 layers. For filamentary switching, the V_O filament formation and rupture occur near the bottom electrode. Scanning Electron Microscopy (SEM) images of fabricated **b.** 16×16 crossbar array **c.** single trilayer RRAM device, and **d.** cross-section of a half-cut RRAM device. Filamentary switching characteristics of **e.** S1 and **f.** S2. **g.** Coexistence of filamentary and bulk switching RRAM in S3. They show the opposite polarity due to the different resistance-switching mechanisms. **h.** Bulk RRAM DC I-V characteristics of S4 without forming filaments. 50 cycles of DC sweeps perfectly overlap, showing highly uniform bulk switching.

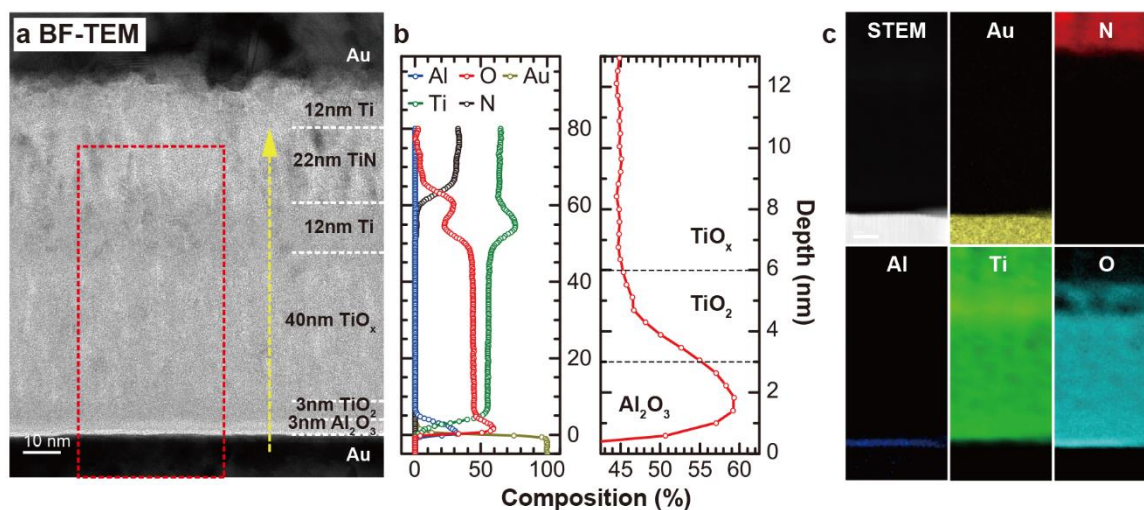


Figure 2. Cross-sectional analysis of bulk RRAM device. a. Cross-sectional bright-field Transmission Electron Microscopy (TEM) image of trilayer bulk RRAM. The bright contrast of TiO_x suggests a porous structure for the layer. **b.** Atomic concentration profile measured by Scanning Transmission Electron Microscopy – Electron Energy Loss Spectroscopy (STEM-EELS) along the yellow arrow. All interfaces were determined based on the ion concentration and contrast in TEM image. The sputtered TiO_x layer shows a smaller oxygen concentration which is lower than ALD TiO₂ layer due to the V_O in the layer. **c.** STEM-EELS mapping of red dotted box region in **a.**

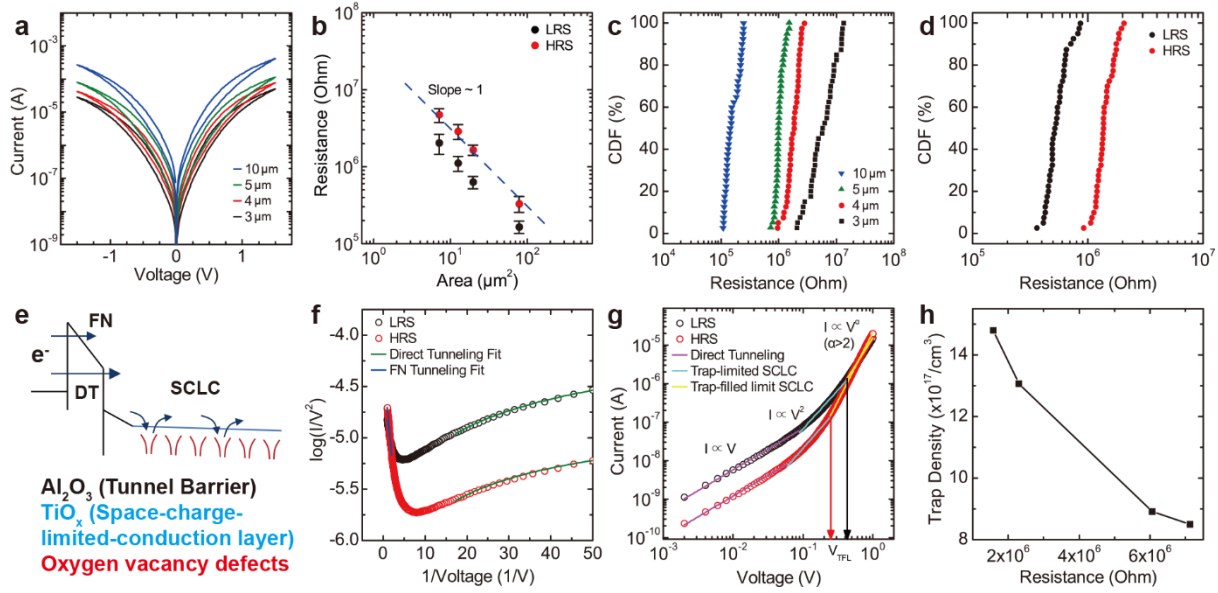


Figure 3. Electrical DC characterization of bulk RRAM devices. **a.** DC I-V switching curves of trilayer bulk RRAM with different diameter cells from $3\mu\text{m}$ to $10\mu\text{m}$. **b.** Double log plot of resistance vs. cell area. Area-scaling behaviour with a slope of 1 suggests bulk switching of RRAM devices. Each size cell data is collected from 40 different devices measured at $V_{\text{read}} = 0.1\text{V}$. **c.** Cumulative distribution function (CDF) of bulk RRAM pristine resistance in different size cells. **d.** CDF of LRS and HRS states programmed with DC sweep using bulk RRAM $5\mu\text{m}$ devices. **e.** Band diagram of trilayer bulk RRAM. Al_2O_3 3nm wide gap layer acts as a tunneling barrier where the direct/Fowler-Nordheim (FN) tunneling happen at small/large voltage region. In the TiO_x layer, space-charge-limited-conduction (SCLC) occurs due to deep-level V_{O} defects. **f.** $\text{Log}(I/V^2)$ vs. $1/V$ curves of high resistance state (HRS) and low resistance state (LRS). Both states show similar conduction mechanism. **g.** $\text{Log } I - \text{log } V$ plot of LRS and HRS states. From the SCLC fitting, trap-filled-limited voltage (V_{TFL}) can be achieved. In the trap-limited conduction region, the current is proportional to V^2 . When the trap filling happens, the current starts to increase rapidly so that the current is proportional to V^α ($\alpha > 2$). **h.** Trap density (N_t) vs. device resistance curve. N_t is calculated by the following equation. $V_{\text{TFL}} = qN_tL^2/2\epsilon$. q is an elementary charge, N_t is a trap density, L is a layer thickness, and ϵ is a dielectric constant.

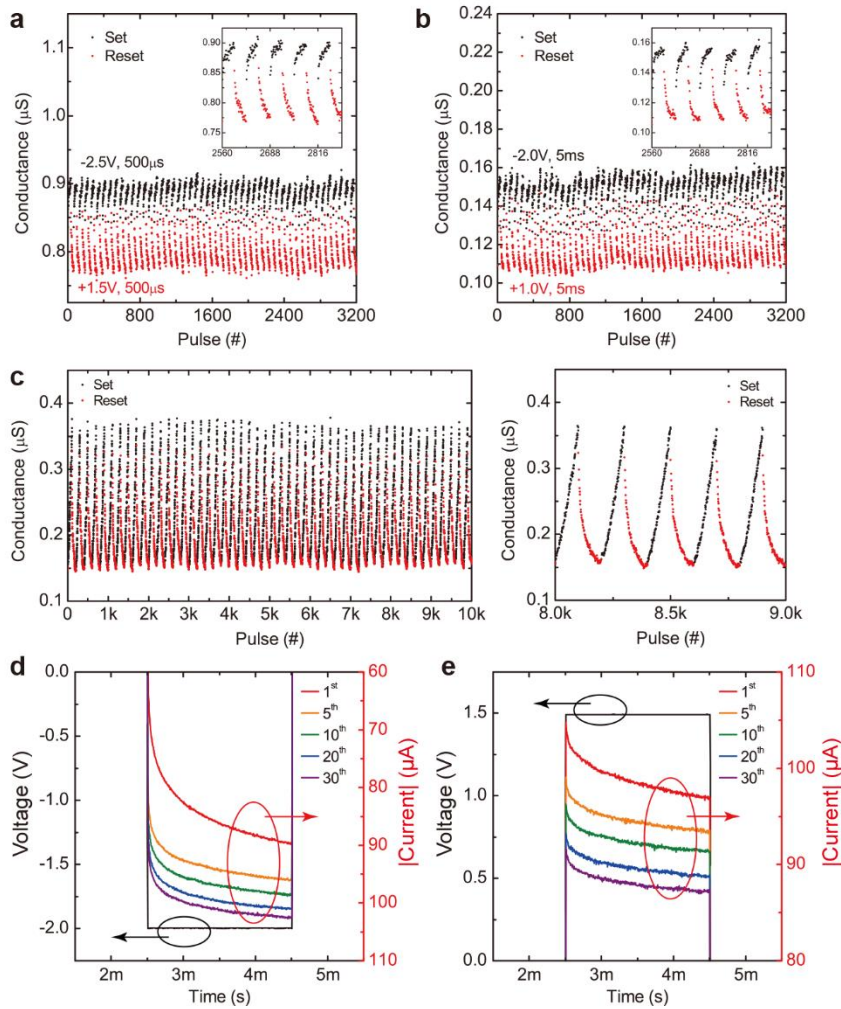


Figure 4. Multilevel gradual switching characteristics of the bulk RRAM devices using pulse measurements. **a.** Multilevel switching using an identical pulse scheme for 32 different states. Set: -2.5V, 500µs / Reset: +1.5V, 500µs. **b.** Multilevel switching using an identical pulse scheme for 32 different states. Set: -2.0V, 5ms / Reset: +1.0V, 5ms. **c.** Multilevel switching using an identical pulse scheme for 100 states. Set: -0.8V to -2.78V (-20mV step) / Reset: +0.3V to +0.993V (+7mV step). The transient current measurements using identical pulses **d.** set (-2V) and **e.** reset (+1.5V) operations showing multi-level bulk switching without any abrupt current jumps (no filaments).

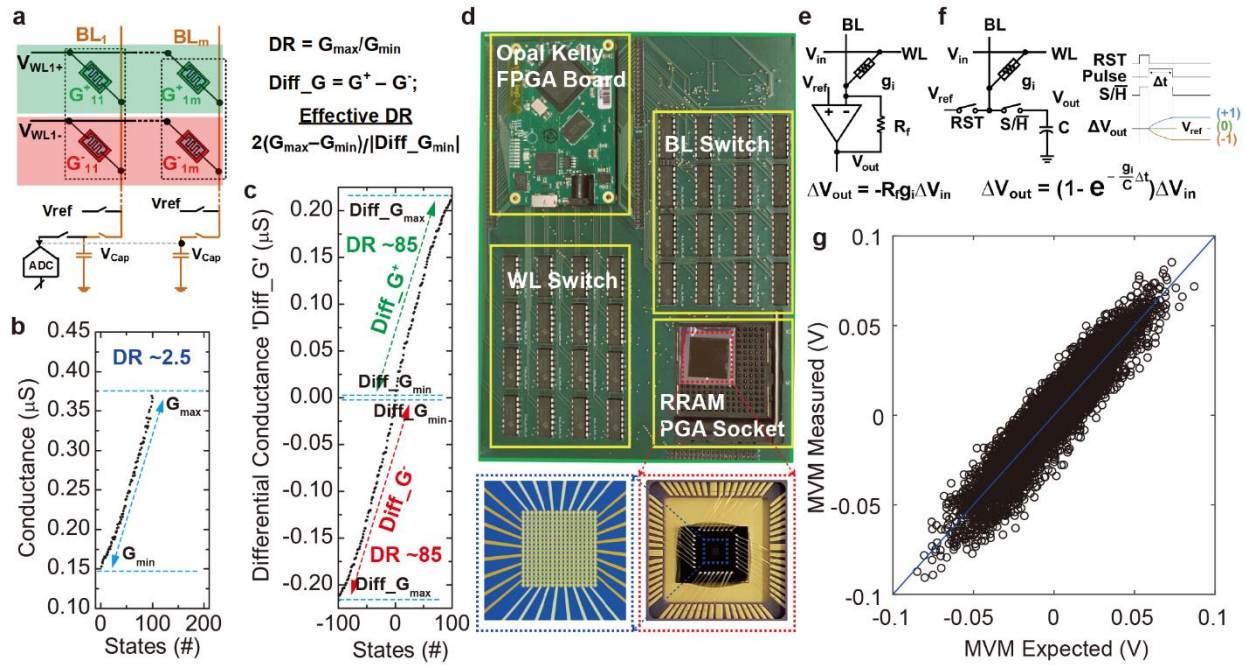


Figure 5. Row-differential voltage sensing using neuromorphic compute-in-memory platform with packaged bulk RRAM crossbar. **a.** Row-differential scheme. Two RRAMs sharing the same column represent positive and negative weights by applying opposite polarity voltage to respective WLs. **b.** Dynamic range for switching for bulk RRAM. **c.** Dynamic range enhancement using the row-differential scheme. For 100 levels, the row-differential scheme can increase the effective dynamic range up to ~170. **d.** Photograph of neuromorphic compute-in-memory board with packaged bulk RRAM crossbar. **e.** Conventional current sensing using transimpedance amplifier. **f.** Switched-capacitor voltage-sensing circuit to achieve higher energy efficiency. **g.** Measured and expected MVM outputs for the differential encoding.

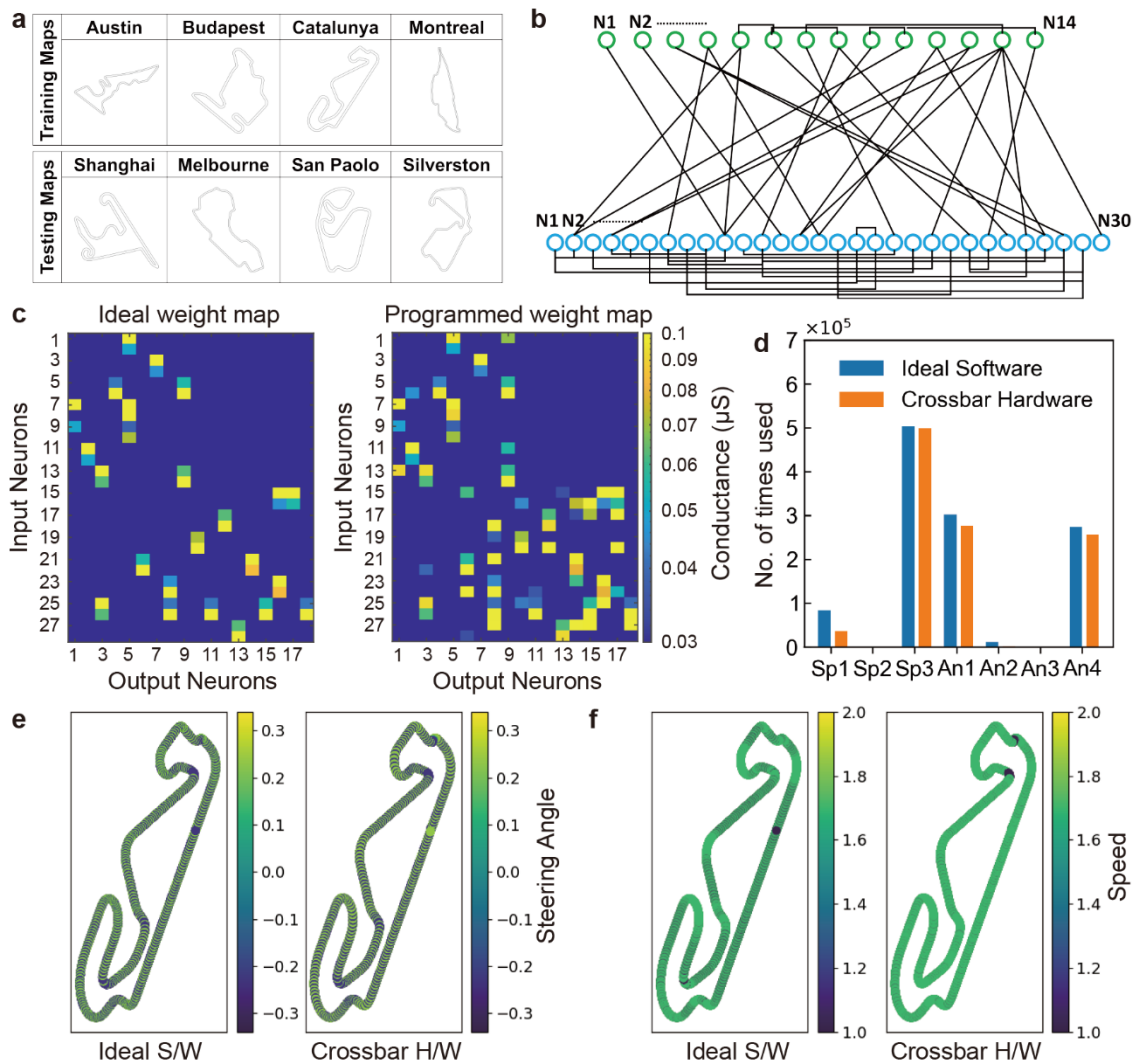


Figure 6. Hardware implementation of SNN for a navigation/racing task. **a.** Examples of training and testing racetracks for navigation tasks. **b.** Schematics of trained SNN (14 input / 30 output neurons) **c.** Weight map comparison between ideal weights and experimentally programmed weights on crossbars using the row-differential encoding. Two 16x16 crossbars were used for weight mapping. **d.** Number of speed (Sp = 1, 1.6, 1.7) and steering angle (An = -0.23, 0, 0.17, 0.23) computations across navigation through all fifteen racetracks. Ideal software simulation and crossbar hardware implementation show highly consistent results. (Fitness score: 0.54 (Ideal S/W) vs. 0.43 (Crossbar H/W)). Ideal software vs. crossbar hardware computation of **e.** steering angle and **f.** speed during testing in the Catalunya map.

References

- 1 Schuman, C. D. *et al.* Opportunities for neuromorphic computing algorithms and applications. *Nature Computational Science* **2**, 10-19 (2022).
- 2 Jouppi, N. P. *et al.* in *Proceedings of the 44th annual international symposium on computer architecture*. 1-12.
- 3 Keckler, S. W., Dally, W. J., Khailany, B., Garland, M. & Glasco, D. GPUs and the future of parallel computing. *IEEE micro* **31**, 7-17 (2011).
- 4 Oh, S., Huang, Z., Shi, Y. & Kuzum, D. The impact of resistance drift of phase change memory (PCM) synaptic devices on artificial neural network performance. *IEEE Electron Device Letters* **40**, 1325-1328 (2019).
- 5 Shi, Y. *et al.* Performance prospects of deeply scaled spin-transfer torque magnetic random-access memory for in-memory computing. *IEEE Electron Device Letters* **41**, 1126-1129 (2020).
- 6 Shi, Y. *et al.* Neuroinspired unsupervised learning and pruning with subquantum CBRAM arrays. *Nature communications* **9**, 5312 (2018).
- 7 Oh, S. *et al.* Energy-efficient Mott activation neuron for full-hardware implementation of neural networks. *Nature Nanotechnology* **16**, 680-687 (2021).
- 8 Jerry, M. *et al.* in *2017 IEEE international electron devices meeting (IEDM)*. 6.2. 1-6.2. 4 (IEEE).
- 9 Kim, H., Mahmoodi, M., Nili, H. & Strukov, D. B. 4K-memristor analog-grade passive crossbar circuit. *Nature communications* **12**, 5198 (2021).
- 10 Wang, Q., Wang, X., Lee, S. H., Meng, F.-H. & Lu, W. D. in *2019 IEEE international electron devices meeting (IEDM)*. 14.14. 11-14.14. 14 (IEEE).
- 11 Schranghamer, T. F., Oberoi, A. & Das, S. Graphene memristive synapses for high precision neuromorphic computing. *Nature communications* **11**, 5474 (2020).
- 12 Ge, R. *et al.* Atomristor: nonvolatile resistance switching in atomic sheets of transition metal dichalcogenides. *Nano letters* **18**, 434-441 (2018).
- 13 Seo, S. *et al.* Artificial van der Waals hybrid synapse and its application to acoustic pattern recognition. *Nature communications* **11**, 3936 (2020).
- 14 Christensen, D. V. *et al.* 2022 roadmap on neuromorphic computing and engineering. *Neuromorphic Computing and Engineering* **2**, 022501 (2022).
- 15 Wan, W. *et al.* in *2020 IEEE International Solid-State Circuits Conference-(ISSCC)*. 498-500 (IEEE).
- 16 Wan, W. *et al.* A compute-in-memory chip based on resistive random-access memory. *Nature* **608**, 504-512 (2022).
- 17 Raghavan, N. *et al.* in *2013 IEEE International Electron Devices Meeting*. 21.21. 21-21.21. 24 (IEEE).
- 18 Kim, S. *et al.* 4-bit Multilevel Operation in Overshoot Suppressed Al₂O₃/TiO_x Resistive Random-Access Memory Crossbar Array. *Advanced Intelligent Systems* **4**, 2100273 (2022).
- 19 Rao, M. *et al.* Thousands of conductance levels in memristors integrated on CMOS. *Nature* **615**, 823-829 (2023).
- 20 Chen, A. A comprehensive crossbar array model with solutions for line resistance and nonlinear device characteristics. *IEEE Transactions on Electron Devices* **60**, 1318-1326 (2013).
- 21 Xia, Q. & Yang, J. J. Memristive crossbar arrays for brain-inspired computing. *Nature materials* **18**, 309-323 (2019).
- 22 Yu, L.-E., Kim, S., Ryu, M.-K., Choi, S.-Y. & Choi, Y.-K. Structure Effects on Resistive Switching of Al/TiO_x/Al Devices for RRAM Applications. *IEEE electron device letters* **29**, 331-333 (2008).
- 23 Zhang, H. *et al.* Understanding the coexistence of two bipolar resistive switching modes with opposite polarity in Pt/TiO₂/Ti/Pt nanosized ReRAM devices. *ACS applied materials & interfaces* **10**, 29766-29778 (2018).

- 24 Park, J., Yoon, H., Sim, H., Choi, S.-Y. & Son, J. Accelerated hydrogen diffusion and surface exchange by domain boundaries in epitaxial VO₂ thin films. *ACS nano* **14**, 2533-2541 (2020).
- 25 Navickas, E. *et al.* Fast oxygen exchange and diffusion kinetics of grain boundaries in Sr-doped LaMnO₃ thin films. *Physical Chemistry Chemical Physics* **17**, 7659-7669 (2015).
- 26 Padovani, A., Larcher, L., Pirrotta, O., Vandelli, L. & Bersuker, G. Microscopic modeling of HfO_x RRAM operations: From forming to switching. *IEEE Transactions on electron devices* **62**, 1998-2006 (2015).
- 27 Kim, M. *et al.* Filamentary and interface-type memristors based on tantalum oxide for energy-efficient neuromorphic hardware. *ACS applied materials & interfaces* **14**, 44561-44571 (2022).
- 28 Fantini, A. *et al.* in *2013 5th IEEE International Memory Workshop*. 30-33 (IEEE).
- 29 Park, J. *et al.* Conduction mechanism effect on physical unclonable function using Al₂O₃/TiO_x memristors. *Chaos, Solitons & Fractals* **152**, 111388 (2021).
- 30 Govoreanu, B. *et al.* in *2013 IEEE International Electron Devices Meeting*. 10.12. 11-10.12. 14 (IEEE).
- 31 Shi, Y. *et al.* Integration of Ag-CBRAM crossbars and Mott ReLU neurons for efficient implementation of deep neural networks in hardware. *Neuromorphic Computing and Engineering* **3**, 034007 (2023).
- 32 Kim, S., Jeong, H. Y., Choi, S.-Y. & Choi, Y.-K. Comprehensive modeling of resistive switching in the Al/TiO_x/TiO₂/Al heterostructure based on space-charge-limited conduction. *Applied Physics Letters* **97** (2010).
- 33 Wu, Y. *et al.* in *2022 International Electron Devices Meeting (IEDM)*. 18.14. 11-18.14. 14 (IEEE).
- 34 Jain, S. *et al.* in *2023 IEEE International Symposium on Circuits and Systems (ISCAS)*. 1-4 (IEEE).
- 35 Schuman, C. D., Mitchell, J. P., Patton, R. M., Potok, T. E. & Plank, J. S. in *Proceedings of the 2020 Annual Neuro-Inspired Computational Elements Workshop*. 1-9.
- 36 Schuman, C. *et al.* Evolutionary vs imitation learning for neuromorphic control at the edge. *Neuromorphic Computing and Engineering* **2**, 014002 (2022).
- 37 https://github.com/fltenth/fltenth_racetracks.
- 38 Plank, J., Schuman, C., Bruer, G., Dean, M. & Rose, G. (2018).
- 39 O'Kelly, M., Zheng, H., Karthik, D. & Mangharam, R. Fltenth: An open-source evaluation environment for continuous control and reinforcement learning. *Proceedings of Machine Learning Research* **123** (2020).